

Article

The Influence of Disused ZSM-5 on the Performance of Phosphogypsum-Based Autoclaved Aerated Concrete

Hao Zhou ¹, Jiaqing Wang ², Yang Jiang ³, Ruihuan Liang ⁴, Bing Ma ¹, Houhu Zhang ¹, Binbin Qian ^{5,*} and Yueyang Hu ^{4,*}

¹ Nanjing Institute of Environmental Sciences, Ministry of Ecology and Environment of the People's Republic of China, Nanjing 210042, China; zhouhao@nies.org (H.Z.); myyanb@aliyun.com (B.M.); zhh@nies.org (H.Z.)

² College of Civil Engineering, Nanjing Forestry University, Nanjing 210037, China; jiaqingw@njfu.edu.cn

³ Advanced Green-Materials Institute of China Energy Engineering Corporation, Beijing 100022, China; jiangyang@hotmail.com

⁴ College of Materials Science and Engineering, Yancheng Institute of Technology, Yancheng 224000, China; liangrh1010@163.com

⁵ School of Chemistry and Environmental Engineering, Yancheng Teachers University, Yancheng 224002, China

* Correspondence: qianbb@yctu.edu.cn (B.Q.); huyueyang1989@ycit.edu.cn (Y.H.)

Abstract: Zeolite Socony Mobil-5 (ZSM-5) is a commonly spent catalyst in the petrochemical industry; and phosphogypsum (PG) is a kind of industrial waste produced in the process of phosphoric acid production. The environmental issues caused by these two solid wastes are urgent and thus sustainable methodologies are required to dispose of and reutilize them. In this research, the waste ZSM-5 and waste PG were used to prepare a novel autoclaved aerated concrete. The effects of the different contents of disused ZSM-5 on the microstructures and performance of the PG-based AAC were determined. The results showed that the compressive strength and bulk density of the DZ4 sample were 2.6 MPa and 520 kg/m³, respectively. This study provides a novel and green approach to the reutilization of both waste PG and spent ZSM-5.

Keywords: waste PG; disused ZSM-5; mechanical properties; hardened matrix microstructure



Citation: Zhou, H.; Wang, J.; Jiang, Y.; Liang, R.; Ma, B.; Zhang, H.; Qian, B.; Hu, Y. The Influence of Disused ZSM-5 on the Performance of Phosphogypsum-Based Autoclaved Aerated Concrete. *Buildings* **2023**, *13*, 3012. <https://doi.org/10.3390/buildings13123012>

Academic Editor: Abdelhafid Khelidj

Received: 4 October 2023

Revised: 14 November 2023

Accepted: 20 November 2023

Published: 2 December 2023



Copyright: © 2023 by the authors. Licensee MDPI, Basel, Switzerland. This article is an open access article distributed under the terms and conditions of the Creative Commons Attribution (CC BY) license (<https://creativecommons.org/licenses/by/4.0/>).

1. Introduction

Autoclaved aerated concrete (AAC) has received widespread attention and is commonly applied in load-bearing walls and maintenance filling structures. Compared with traditional concrete blocks, AAC has lower energy costs. Moreover, some distinguished properties of AAC include its light weight, excellent heat preservation, non-combustibility, and good sound insulation [1–3]. AAC is composed of siliceous and calcareous materials after grinding and mixing with gas-generating agents (e.g., Al powder) and other admixtures (e.g., gypsum). The two most common types of AAC used by far are fly ash-based and quartz sand-based AAC [4]. For the preparation of these two types of AAC, the siliceous raw materials are quartz sand and fly ash mixed with the appropriate amount of cement and lime and sufficient water to make a fresh slurry [4–6].

The autoclaving technique directly determines the mechanical properties of AAC and is a key stage in the process of improving the strength of the AAC product. The autoclave stage requires high temperature and pressure [5,7]. For the typical fly ash-based AAC, the approximate curing temperature and pressure are 175–213 °C and 0.9–2.2 MPa, respectively [7–9]. The important improvements in the AAC product after autoclaving include a decrease in ambient curing time that makes the products ready for use after 24 h, a reduction in moisture content, and diminished shrinkage [9,10]. Moreover, the hydration product is changed during the autoclaving process, which is the primary factor in the increased strength of the final product. In the initial stage of autoclaving, calcium silicate hydrate (C-S-H) is formed and subsequently converted into a crystalline product named α -C₂SH, which reduces the strength of the material, as previously reported. However, further

extending the autoclave time transforms α -C₂SH into tobermorite due to the presence of silica and enhances the strength of the AAC [10,11].

In recent years, the exploitation of quartz sand has been extremely restricted in China due to ecological environmental protection; meanwhile, fly ash is being heavily consumed in the building materials industry [4]. Thus, finding alternative raw materials is essential for the preparation of AAC. Many studies have confirmed that industrial waste can be used as feedstock for AAC production, such as graphite tailings, iron ore tailings, blast furnace slag, steel-making slag, waste red gypsum, and zeolites [4,11–15]. There are also some other types of mining waste which could be utilized within concrete composites of different purposes [16,17]. The production of AAC from industrial waste not only addresses the shortage of raw materials but also allows for the secondary utilization of solid waste.

As a major industrial by-product, phosphogypsum (PG) is generated during the production of wet process phosphoric acid. In China, about 300 tons of PG are being stored in open environments, sometimes even in areas of human activity, which poses a risk to both the ecological environment and human health [18–20]. To mitigate the harmful effects of waste PG, PG has been widely used in the building materials industry. Some researchers have used PG to prepare a type of solidified material [21]. Yang et al. prepared a type of load-bearing brick by utilizing autoclaved PG [22]. In particular, the usage of gypsum in the manufacture of AAC has been widely established. Some studies have noted that the addition of gypsum affects the formation of tobermorite and that gypsum will convert into anhydrite after autoclaving and strengthen the AAC product [8,15,23]. Cai et al. prepared a type of AAC through red gypsum and fly ash, and the final product met the standard [15]. Waste PG mainly contains gypsum (CaSO₄·2H₂O), and the properties of waste PG are similar to those of gypsum [20,24]. Therefore, using waste PG in the preparation of AAC is promising and provides an alternative raw material for the requirement of the preparation of AAC.

In the late 1960s, the U.S. Mobil Oil Company synthesized a new type of zeolite molecular sieve named Zeolite Socony Mobil-5 (ZSM-5), which is widely used as a catalyst in the petrochemical industry [25,26]. Due to its unique framework structure and chemical composition, it has many excellent properties, such as a high surface area, microporous channels, thermal stability, hydrophobicity, and acid resistance [27,28]. Furthermore, ZSM-5 has a high silicon-to-aluminum ratio, which results in a particularly high silicon content in ZSM-5 [29]. In general, the micropores in ZSM-5 are blocked after use and form disused ZSM-5. The disused ZSM-5 was landfilled directly, which caused environmental pollution and a waste of resources [7,30]. However, the disused ZSM-5 contains a large amount of original ZSM-5, and some mesopores have a strong foaming ability [11,30,31]. The foaming ability of disused ZSM-5 has been extensively demonstrated. Shao et al. prepared a micropore-foamed geopolymer by using disused ZSM-5, red mud, and fly ash, which reduced the bulk density of the resultant material [26]. Some researchers produced a type of geopolymer using disused ZSM-5 and metakaolin as the raw materials, and the addition of disused ZSM-5 promoted the foaming process of the geopolymer and formed a multiscale pore structure in the geopolymer [30]. Hence, the preparation of AAC using disused ZSM-5 can improve the foaming effect in the final product. In addition, disused ZSM-5 contains large amounts of silicon [26,32], which allows for the substitution of fly ash with disused ZSM-5 as a siliceous raw material in AAC production. Although the application of disused ZSM-5 in autoclaved aerated concrete has been reported, there still exists a research gap in the application of disused ZSM-5 in PG-based autoclaved aerated concrete.

In this study, a novel AAC was developed using cement, fly ash, lime, waste PG, and disused ZSM-5. The samples were characterized after autoclaving to explore the influence of disused ZSM-5 on the hydration products, mechanical properties, and porosity of the AAC product. Finally, the influence of disused ZSM-5 on the formation of tobermorite was studied.

2. Materials and Methods

2.1. Materials

Waste PG (Jinan Xinghong Chemical Co., Ltd., Jinan, China), disused ZSM-5 (Qingdao Hengxintian New Materials Technology Co., Ltd., Qingdao, China), Cement P·O 42.5 (Jiangsu Province Renzhou Cement Co., Ltd., Yancheng, China), fly ash (Yancheng Hengli Fly Ash Development and utilization Co., Ltd., Yancheng, China), and lime and Al powder (Jiangsu Fenghua Chemical Industry Co., Ltd., Yancheng, China) were used. The oxide compositions of waste PG, disused ZSM-5, and fly ash are shown in Table 1 (determined by X-ray fluorescence). Notably, silicon dioxide is abundant in disused ZSM-5. The particle size distributions of fly ash, waste PG, and disused ZSM-5 are exhibited in Figure 1. The D50 and D90 values of the fly ash waste PG and disused ZSM-5 as shown in Table 2. Figure 2 shows the X-ray diffraction (XRD) patterns of the waste PG and disused ZSM-5. The waste PG contained mainly gypsum ($\text{CaSO}_4 \cdot 2\text{H}_2\text{O}$) and bassanite ($\text{CaSO}_4 \cdot 0.5\text{H}_2\text{O}$), and the disused ZSM-5 contained a large quantity of the original ZSM-5. The fly ash broad hump appeared at $17\text{--}29^\circ 2\theta$, which indicates the existence of an amorphous phase.

Table 1. Oxide compositions of the raw materials.

Oxides	Fly Ash	Waste PG	Cement	Disused ZSM-5
SiO_2	52.99	3.67	21.70	94.23
Al_2O_3	30.93	0.23	5.75	0.48
Fe_2O_3	4.34	0.20	2.78	0.21
TiO_2	2.20	0.01	0.28	-
CaO	3.27	31.31	61.31	0.13
MgO	1.51	0.03	2.50	1.29
SO_3	0.27	42.94	3.44	-
$\text{K}_2\text{O} + \text{Na}_2\text{O}$	1.96	0.05	0.95	-
P_2O_5	-	0.42	-	-
LOI	2.53	21.14	1.29	3.66

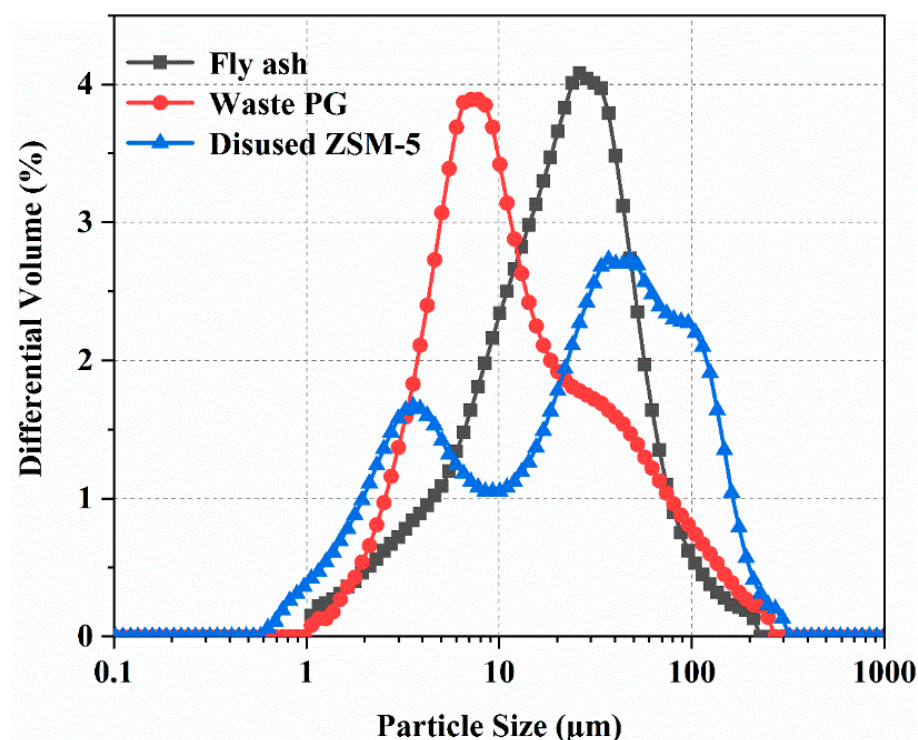
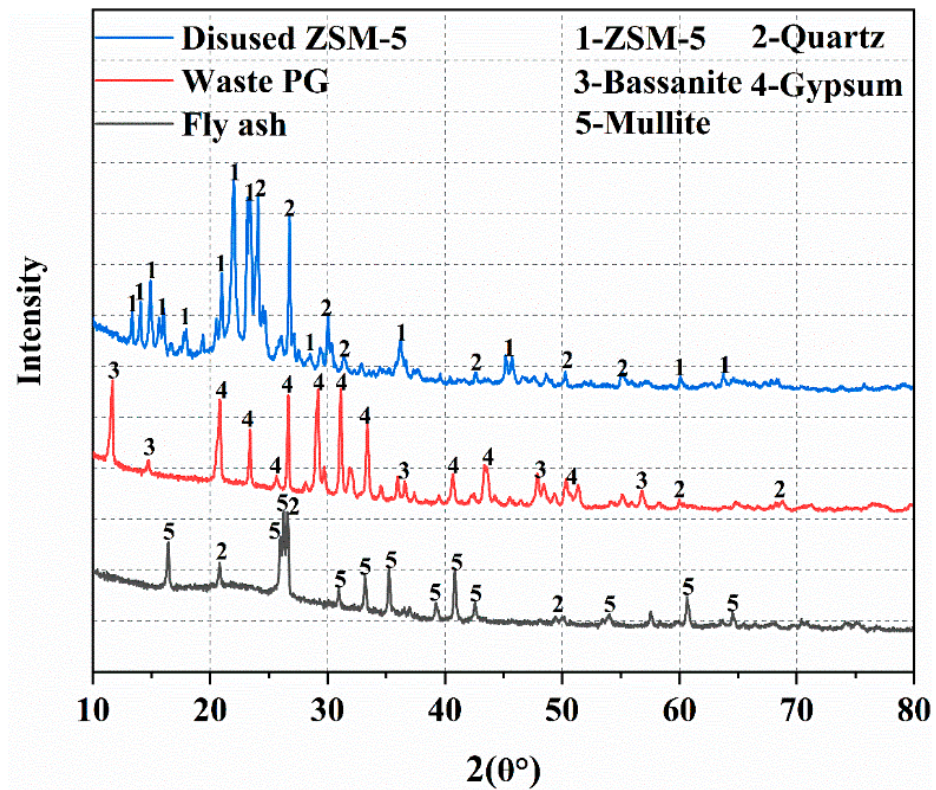


Figure 1. The particle size distributions of the raw materials.

Table 2. The D50 and D90 values of the materials.

Material	D50 (μm)	D90 (μm)
Fly ash	20.4	54.69
Waste PG	9.96	59.50
Disused ZSM-5	26.86	107.6

**Figure 2.** XRD patterns of the raw materials.

2.2. Composition Design of the AAC

The AAC was composed of waste PG, disused ZSM-5, cement, fly ash, lime, and Al powder. The specific raw material mixing ratios are shown in Table 3. The disused ZSM-5 was substituted for fly ash in the sample preparation at contents of 0%, 12.5%, 25%, and 37.5%.

Table 3. Mixing proportions of the raw materials.

Specimen	Cement	Fly Ash	Disused ZSM-5	Waste PG	Lime	Al Powder	W/S
DZ1	21.25%	50%	0%	25%	2.5%	1.25%	1
DZ2	21.25%	37.5%	12.5%	25%	2.5%	1.25%	1
DZ3	21.25%	25%	25%	25%	2.5%	1.25%	1
DZ4	21.25%	12.5%	37.5%	25%	2.5%	1.25%	1

2.3. Characterization

2.3.1. X-ray Diffraction

A powder X-ray diffractometer (D2 PHASER) was used to analyze the mineral phases of the waste PG, disused ZSM-5, fly ash, and AAC products using Cu-K α radiation at a scan rate of 5°/min and a scan range of 5–80°. All tested samples were soaked in anhydrous ethanol for 12 h to stop hydration, and then dried in the drying oven.

2.3.2. Mechanical Tests

A specimen compressive strength test was conducted; the specimens were placed on the side of the calibrated compressive strength testing machine (DL41-3t), and the fixtures were used to stabilize the rate of uniform loading (2400 ± 200 N/s until destruction). The specimens ($100 \text{ mm} \times 100 \text{ mm} \times 100 \text{ mm}$) were numbered 1, 2, 3, and 4.

2.3.3. Bulk Density Test

The bulk density of the products was determined as follows: first, the length of the sample was measured, and the volume was calculated and recorded as V . The test samples were dried at $62 \text{ }^\circ\text{C}$ and $84 \text{ }^\circ\text{C}$ for 24 h each. Next, the test samples were baked at $110 \text{ }^\circ\text{C}$ until the mass remained constant, which was recorded as M . The bulk density of the sample was calculated using the formula below:

$$\text{Bulk density (kg/m}^3\text{)} = \text{constant weight (M)/volume of the product (V)}$$

2.3.4. FT-IR Spectroscopy Test

Fourier transform infrared (FT-IR) was tested using the FTIR-650 analyzer in the range of $400\text{--}4000 \text{ cm}^{-1}$, with a resolution of 4 cm^{-1} .

2.3.5. TG Test

The TGA-601 analyzer was used to analyze the thermogravimetric. The powders were heated from $24 \text{ }^\circ\text{C}$ to $1000 \text{ }^\circ\text{C}$, at rate of $10 \text{ }^\circ\text{C}/\text{min}$, with a nitrogen atmosphere.

2.3.6. MIP Analysis

The pore size distribution and total porosity are two important parameters that can reflect the pore structure of the product. Mercury intrusion porosimetry (MIP) is a common method for determining the pore size distribution and porosity due to its ease of operation. The test principle of MIP is that mercuries enter the pores of the sample at different pressures; measuring the volume of mercury in the pores at different pressures can determine the pore distribution of the sample.

2.3.7. SEM and EDXS Analysis

The micromorphological features and energy dispersive X-ray spectroscopy (EDXS) of the samples were determined by employing scanning electron microscopy (SEM) with an Axia ChemiSEM analyzer (Thermo Fisher Scientific Co., Ltd., Shanghai, China).

3. Results and Discussion

3.1. X-ray Diffraction

The XRD patterns for the samples DZ1–DZ4 before the autoclaving process are displayed in Figure 3a. The major phases are ZSM-5, ettringite, gypsum, bassanite, quartz, calcite, and mullite. Additionally, many peaks occurred at approximately 30° , indicating the presence of the C-S-H gel [33]. Mullite was abundant in DZ1, DZ2, and DZ3 because of the relatively high content of fly ash in the samples, and mullite is one of the main minerals in fly ash [34]. The peak of ettringite appeared in all samples, and ettringite was formed during the hydration of the cement. According to a previous report, the ettringite content increased gradually as the gypsum content increased [35,36]. The addition of waste PG increases the residual gypsum content in the cement hydration process, which promotes the formation of ettringite [35]. Ettringite ensures the early strength of the samples and allows for the easier removal of the samples from the mold. Moreover, the sample incorporating the disused ZSM-5 showed a peak corresponding to ZSM-5, which was due to the presence of a small amount of unreacted disused ZSM-5. In addition, the sample containing disused ZSM-5 exhibited a peak corresponding to quartz at approximately $21\text{--}22^\circ$; a similar result was reported by Shao et al. [31]. Gil et al. found that the desilication of disused ZSM-5 occurred under alkaline conditions, resulting in the removal of silica from the disused

ZSM-5 framework [37]. Bassanite was the mineral phase contained in waste PG; notably, the peak for bassanite was not observed in DZ1. Usually, gypsum can excite the activity of the glass structure in fly ash at some temperatures [38,39]. Because DZ1 contained the largest amount of fly ash, more gypsum reacted and the bassanite peak was absent. As the amount of fly ash in the sample decreased, the amount of reacted gypsum diminished; thus, the residual gypsum increased, and bassanite was present in the sample. Calcite was noted in all samples due to the partial carbonization of the samples in the preparation process.

Figure 3b exhibits the XRD patterns of the samples after autoclaving. The crystalline phases are tobermorite, ZSM-5, bassanite, mullite, quartz, anhydrite, and calcite. Notably, the peak corresponding to ettringite disappeared, and a similar result was reported by another study. The decomposition of ettringite occurred at approximately 50–110 °C [40]. Compared to the sample before autoclaving, two new minerals appeared: tobermorite and anhydrite. The tobermorite was observed at approximately 7.8°, 29.8°, and 31.7°, and these findings were similar to the results of previous studies [12,15]. The existence of tobermorite enhances the strength of the AAC; in general, C-S-H gel is converted into tobermorite during the autoclaving process. The peak of anhydrite was intense in the samples; anhydrite is the main product of gypsum after autoclaving, which significantly improves the strength of the AAC product [23]. Furthermore, the peaks of mullite and quartz markedly decreased, which were consumed during the autoclaving process.

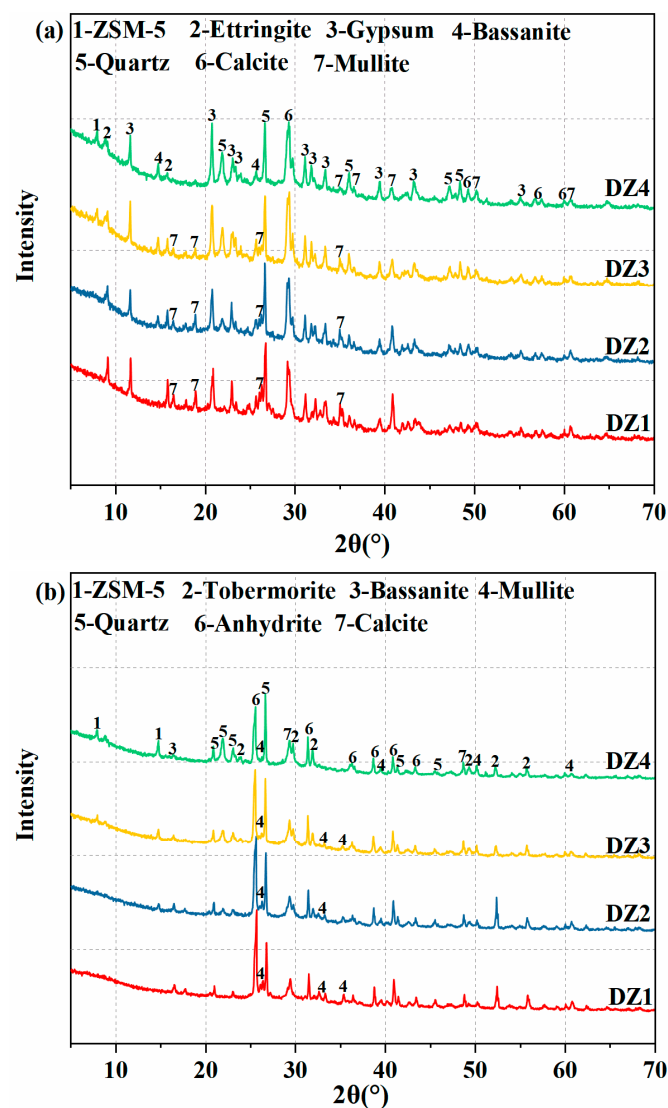


Figure 3. XRD patterns of (a) Z1-Z4 before and (b) after autoclaving.

3.2. The Foaming Property

The foaming effect of AAC is illustrated by the expansion volume of the slurries. Figure 4 shows that the expansion volumes of slurries DZ1, DZ2, DZ3, and DZ4 were 99, 108, 119, and 135 mL, respectively. Notably, the expansion volume of the slurries increased with the addition of disused ZSM-5 because disused ZSM-5 has a strong foaming ability. The foaming mechanism of disused ZSM-5 is as follows: disused ZSM-5 has a large surface area and contains many mesopores, and the air remaining in the disused ZSM-5 pore structure expands during high-temperature curing and forms a porous structure in the sample [41,42]. DZ1, DZ2, and DZ3 expanded rapidly in the first 70 min, and this expansion plateaued after 70 min. Notably, because DZ4 contained the largest amount of ZSM-5, it had only partially expanded after 70 min and exhibited the strongest foaming ability of all the slurries.

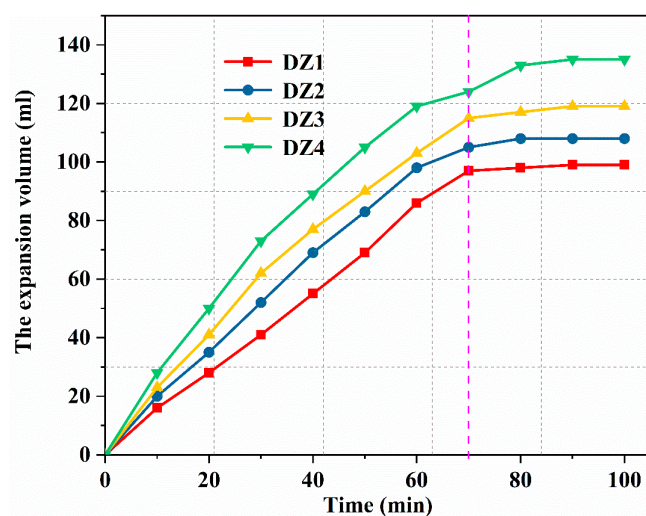


Figure 4. The expansion volume of the slurries.

3.3. Compressive Strength and Bulk Density

Figure 5 exhibits the influence of disused ZSM-5 on the properties of the samples. The bulk densities of DZ1, DZ2, DZ3, and DZ4 were 715, 648, 593, and 520 kg/m³, respectively. As the disused ZSM-5 increased from 0% to 37.5, the bulk density decreased from 715 to 520 kg/m³. Two factors decreased the AAC bulk density. (1) The incorporation of waste ZSM-5 improved the foaming capacity of the slurry, which has been widely confirmed. A stronger foaming effect of the slurry reduces the bulk density of the sample. The air in the disused ZSM-5 mesopores expands during the curing stage, forming a porous structure in the AAC. A higher content of disused ZSM-5 increases the porosity in the final products, leading to lower bulk densities. (2) The bulk densities of the total raw materials also affect the bulk density of the sample. Shao et al. found that a lower bulk density of the total raw materials will reduce the bulk density of the sample [31]. The bulk density of disused ZSM-5 (0.52 g/cm³) is lower than that of fly ash (0.83 g/cm³); as the amount of disused ZSM-5 added increased, the total raw material bulk density decreased, reducing the bulk density of the final sample.

The compressive strengths of DZ1, DZ2, DZ3, and DZ4 were 5.8, 4.5, 3.7, and 2.6 MPa, respectively. The compressive strength slowly decreased from 5.8 MPa to 2.6 MPa, due to the disused ZSM-5 content increasing from 0% to 37.5%. The structure of the sample directly determines the compressive strength, as the strong foaming effect of disused ZSM-5 leads to a less compact structure in the AAC; therefore, a decrease in the compressive strength of the products was observed. Moreover, the compressive strength highly correlates with bulk density, and some studies have shown that a higher bulk density of the sample increases the compressive strength [30,43].

Overall, all samples complied with the standards. The bulk density of DZ1 met the B07 level, DZ2 and DZ3 met the B06 level, and DZ4 met the B05 level. The strength of

all samples also met the standard. Notably, the B05 level of AAC is currently the most used in building materials; PG-based AAC has a high bulk density and the bulk density of DZ1 was close to the limit value of the B07 level. In this study, PG was dosed at 25%, and the addition of disused ZSM-5 significantly reduced the bulk density of the AAC, which broadened the possible applications of the final product.

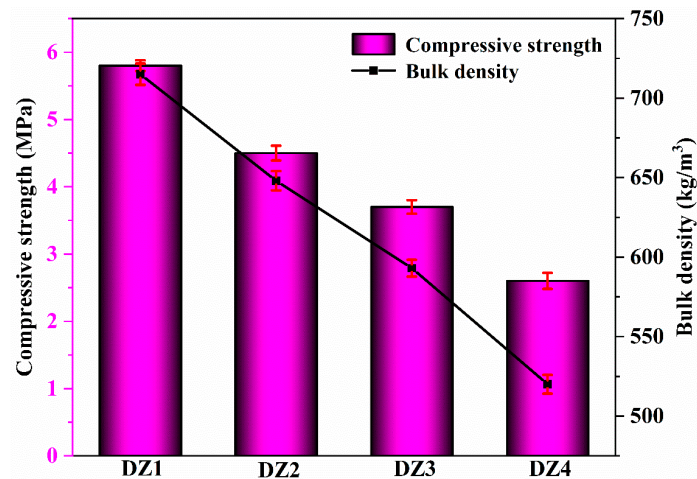


Figure 5. Mechanical performance of the final AAC product.

3.4. FT-IR Analysis

Figure 6 shows the FTIR spectra of the AAC product; it can be well seen that the stretching vibration bands and bending vibration bands correspond to molecular H₂O at approximately 3466–3431 cm⁻¹ and 1659–1627 cm⁻¹, respectively [44]. Generally, water molecules are retained in the structural cavities of the AAC samples. Absorption bands are observed at 1430–1451 cm⁻¹, which are due to the vibrations of CO₃²⁻ and indicate that there was carbon dioxide pollution during the preservation process [45]; the result is consistent with the XRD results, with calcite present in all samples. The bands at 1126–1116 cm⁻¹ are due to Si-O-Al asymmetric stretching vibrations [25]. The sharp peaks between 680 and 666 cm⁻¹ are attributed to the bending vibration modes of sulphate, which are the characteristic peaks of anhydrite [46]. Finally, the bands at 465, 463, 458, and 453 cm⁻¹ are due to the presence of tobermorite [47].

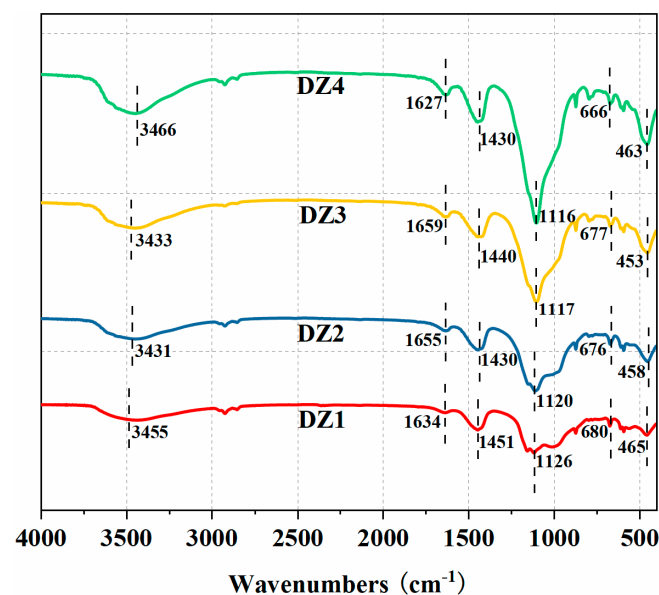


Figure 6. FTIR spectra of the AAC samples.

3.5. TG Analysis

The TG results of the samples are exhibited in Figure 7. The weight losses of DZ1, DZ2, DZ3, and DZ4 are approximately 19%, 15%, 13%, and 12%, respectively. DZ1 exhibited the greatest weight loss. The TG curve shows four significant mass losses. The first weight loss of the AAC appeared at 50–320 °C, mainly attributed to the loss of bound water [7]. Stage II, from 320 to 646 °C, is associated with the water loss of C-S-H (B) as it transforms into C-S-H (A). In addition, water loss from tobermorite also occurs at this stage [11]. During Stage III, mass loss occurs between 646 and 770 °C and corresponds to the decomposition of calcite, and the results are consistent with the XRD analysis [12]. The last weight loss stage from 770–1000 °C is due to the dehydrated C-S-H (B) and tobermorite transforming into wollastonite; meanwhile, the decomposition of anhydrite also contributes to the loss of quality in this section. Notably, DZ1 exhibited the greatest mass loss at 770–1000 °C, indicating that DZ1 contains high levels of tobermorite and anhydrite [15]. DZ1 had the highest content of fly ash, resulting in PG that was reacted the most, making the final products have the highest levels of tobermorite and anhydrite. The presence of tobermorite and anhydrite together contributes to the strength of the AAC, which is the reason for the highest strength of DZ1. DZ4 showed the least weight loss, because the lowest amount of PG was reacted, leading to the final product containing low levels of tobermorite and anhydrite.

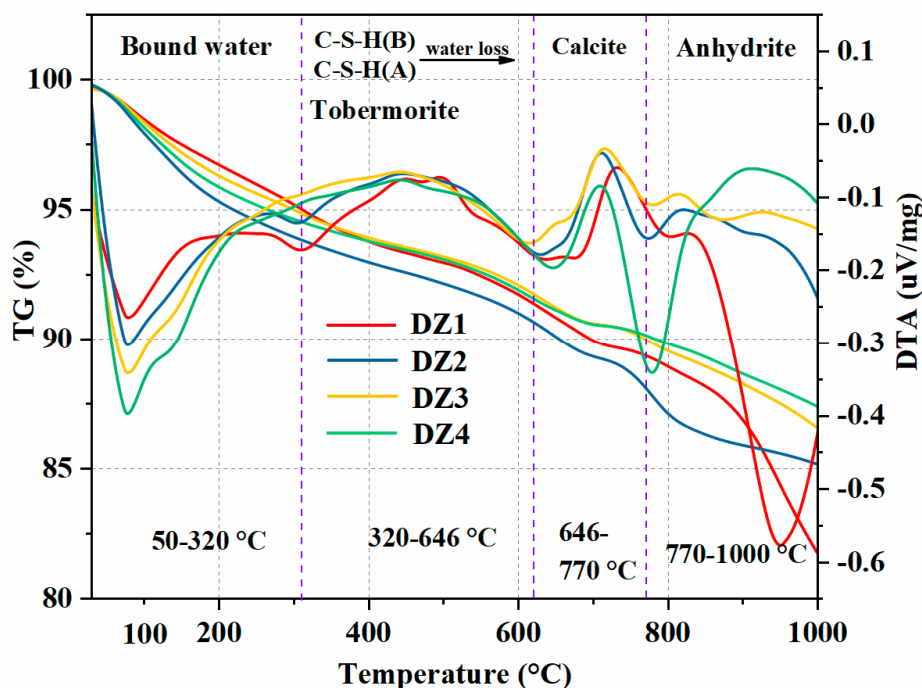


Figure 7. The TG-DTA results of the samples.

3.6. MIP Analysis

Table 4 shows the porosities of the AAC products; the porosities of DZ1, DZ2, DZ3, and DZ4 were 60.24%, 66.71%, 70.81%, and 75.44%, respectively. Notably, the total porosity significantly increased upon the addition of disused ZSM-5 because disused ZSM-5 has a strong foaming ability. The addition of disused ZSM-5 increases the foaming effect of the slurries and increases the porosity of the final AAC product. The cumulative intrusion of mercury is exhibited in Figure 8 and indicates the porosities of the samples. Increasing the content of disused ZSM-5 increased the cumulative intrusion of mercury, which indicates that the samples were more porous.

The pore size distribution table of the samples is shown in Figure 9 and Table 5. The pore size distribution curve of DZ1 is more skewed to the left, indicating that it

contains more small-diameter pores. Small-diameter pores result in a more compact sample structure and improve the sample strength. Compared to the pore diameter distribution graph of DZ1, that of DZ2 is shifted more to the right, indicating that the fraction of small-diameter pores slightly increased. The disused ZSM-5 increased the foaming effect of the slurry, which made the final sample more porous and resulted in some small-diameter pores and partially large-diameter pores. As the disused ZSM-5 content gradually increased, the pore distribution of the samples significantly changed. The curves of DZ3 and DZ4 were most offset to the right, which indicates that the number of large-diameter pores increased (especially pores larger than 52 μm). Large-diameter pores decrease the strength of the sample while also decreasing the bulk density of the AAC, which is the primary reason for adjusting the AAC from the B07 to B05 level. Moreover, DZ3 and DZ4 included many small-diameter pores, which ensures the strength of the products.

In conclusion, the pore structure strongly determines the mechanical properties of AAC products. Small-diameter pores ensure the compressive strength of the products, but an excessive amount of smaller-diameter pores in the sample will result in a high bulk density of the product, which can cause the product to be overweight. The improved foaming effect of the slurry increases the number of large-diameter pores in the product, which decreases the bulk density of the AAC.

Table 4. The total porosity of the AAC.

Sample No.	Porosity (%)
DZ1	60.24
DZ2	66.71
DZ3	70.81
DZ4	75.44

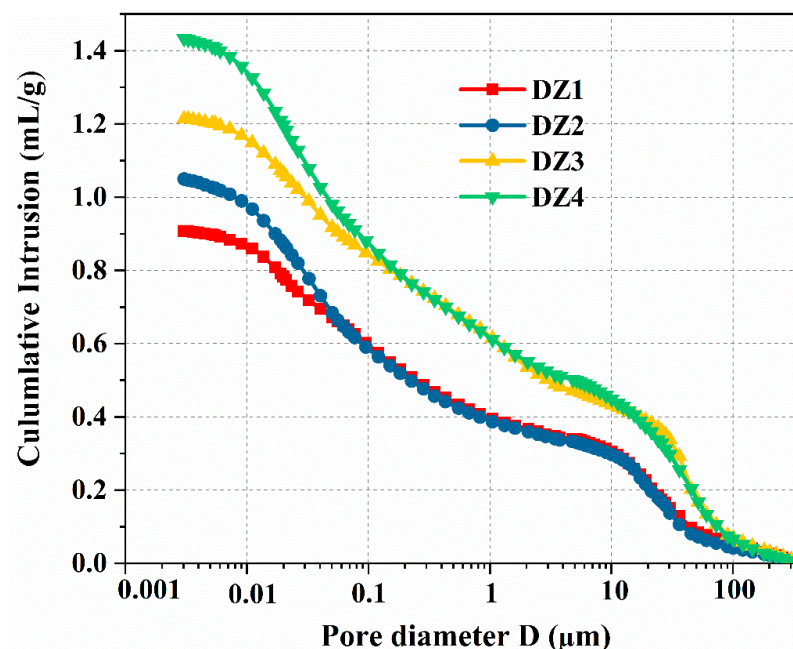


Figure 8. The cumulative intrusion of mercury.

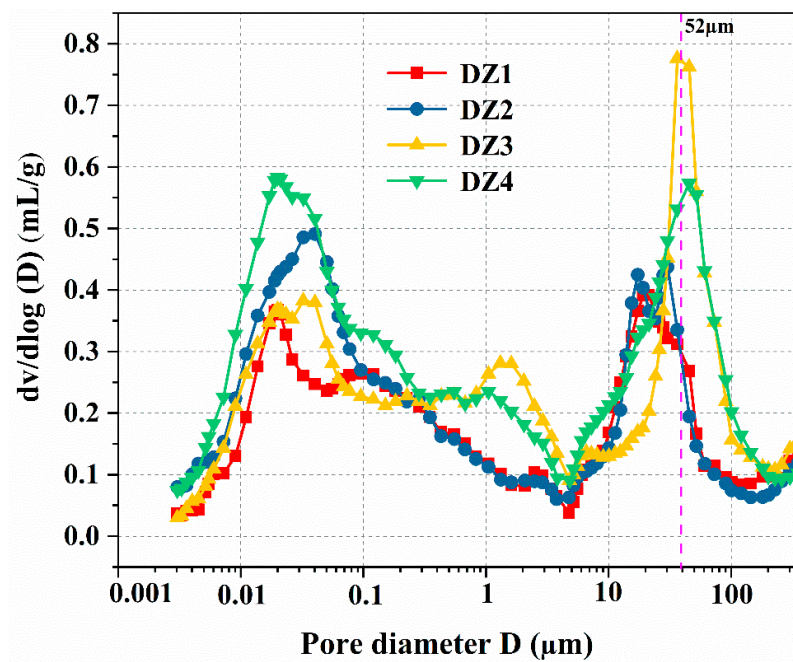


Figure 9. The pore size distribution of the AAC.

Table 5. Pore size distribution table of the samples.

Samples No.	Pore Size Distribution by Volume Ratio (%)		
	<0.1 μm	0.1–52 μm	>52 μm
DZ1	40.2	52.5	7.3
DZ2	37.9	51.4	10.7
DZ3	35.2	51.3	13.5
DZ4	33.7	46.1	20.2

3.7. SEM and EDX Analysis

The micromorphological features and EDX analysis of the AAC are shown in Figure 10. The SEM images of the AAC before autoclaving are exhibited in Figure 10a–h. Figure 10a illustrates the apparent morphology of DZ1. Notably, the sample without adding disused ZSM-5 had a compact structure, and the surface had fewer cracks and pores. The magnified micrograph of DZ1 is shown in Figure 10b, which primarily shows ettringite, strip-like gypsum, and C-S-H. Before the autoclaving process, the existence of ettringite ensures the strength of the AAC, which simplifies its removal from the mold. A large amount of gypsum due to the addition of waste PG is seen, and autoclaving converts this gypsum into anhydrite, which contributes to the strength of the AAC. C-S-H gel is a precursor for the formation of tobermorite during autoclaving. The appearance of DZ2 is exhibited in Figure 10c. The sample containing disused ZSM-5 shows clear pores on the surface. Because of the foaming ability of disused ZSM-5, the porosity of the final products increased, and more pores were consequently observed on the surface. Figure 10d shows the magnified micrograph of DZ2; the main hydration products are ettringite and gypsum. Figure 10e,g exhibits the apparent morphologies of DZ3 and DZ4, respectively. The increased content of the disused ZSM-5 increased the number of pores and reduced the compactness of the AAC. Some large-diameter pores are even observed in DZ3 and DZ4. Magnified micrographs of DZ3 and DZ4 are exhibited in Figure 10f,h, respectively. In addition to gypsum, C-S-H gel, and ettringite, some white spots are noted in DZ3. EDXS (f1) indicated a high silicon content, which is attributed to the presence of unreacted disused ZSM-5; this finding is also consistent with the XRD results.

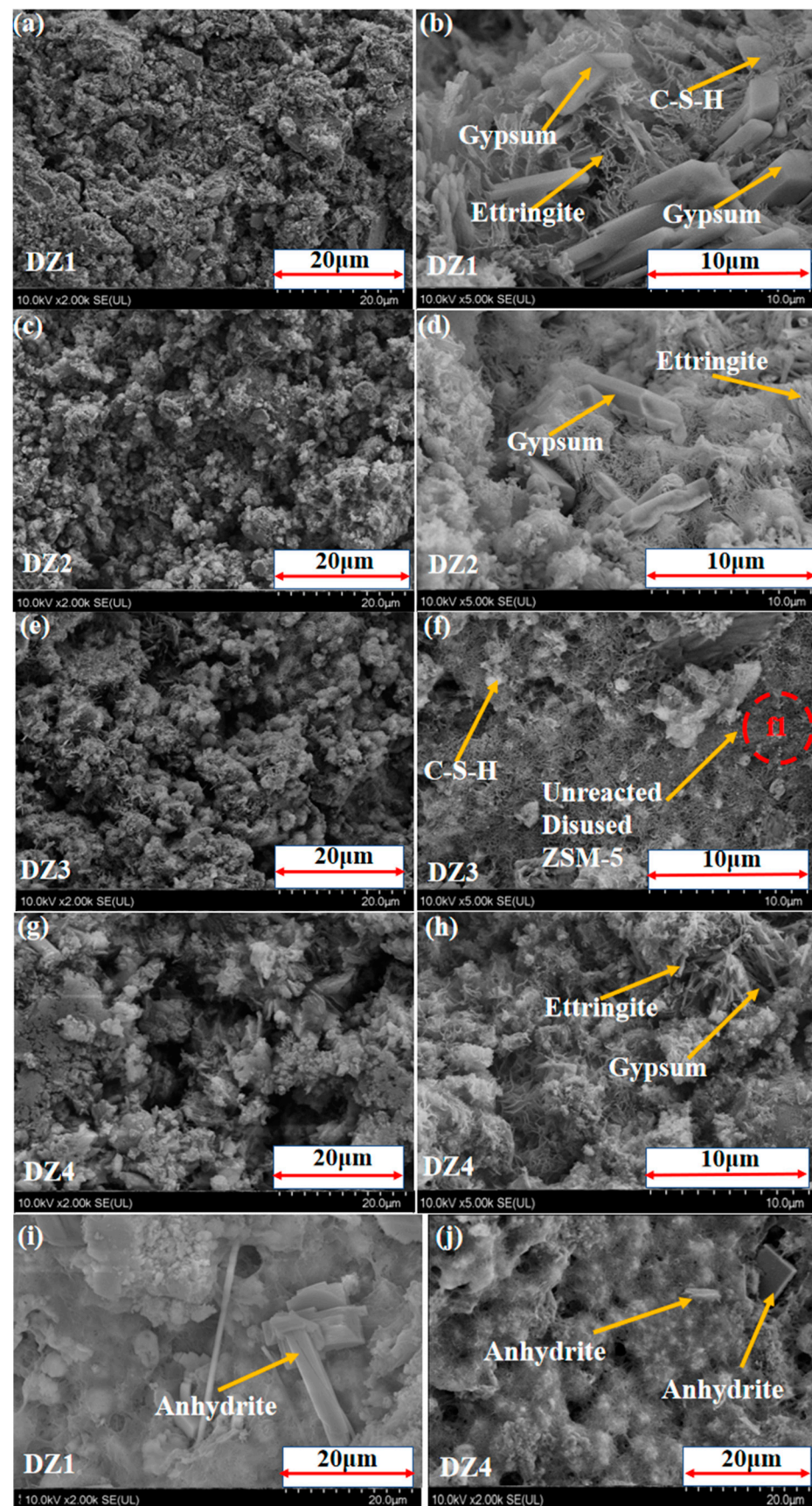


Figure 10. Cont.

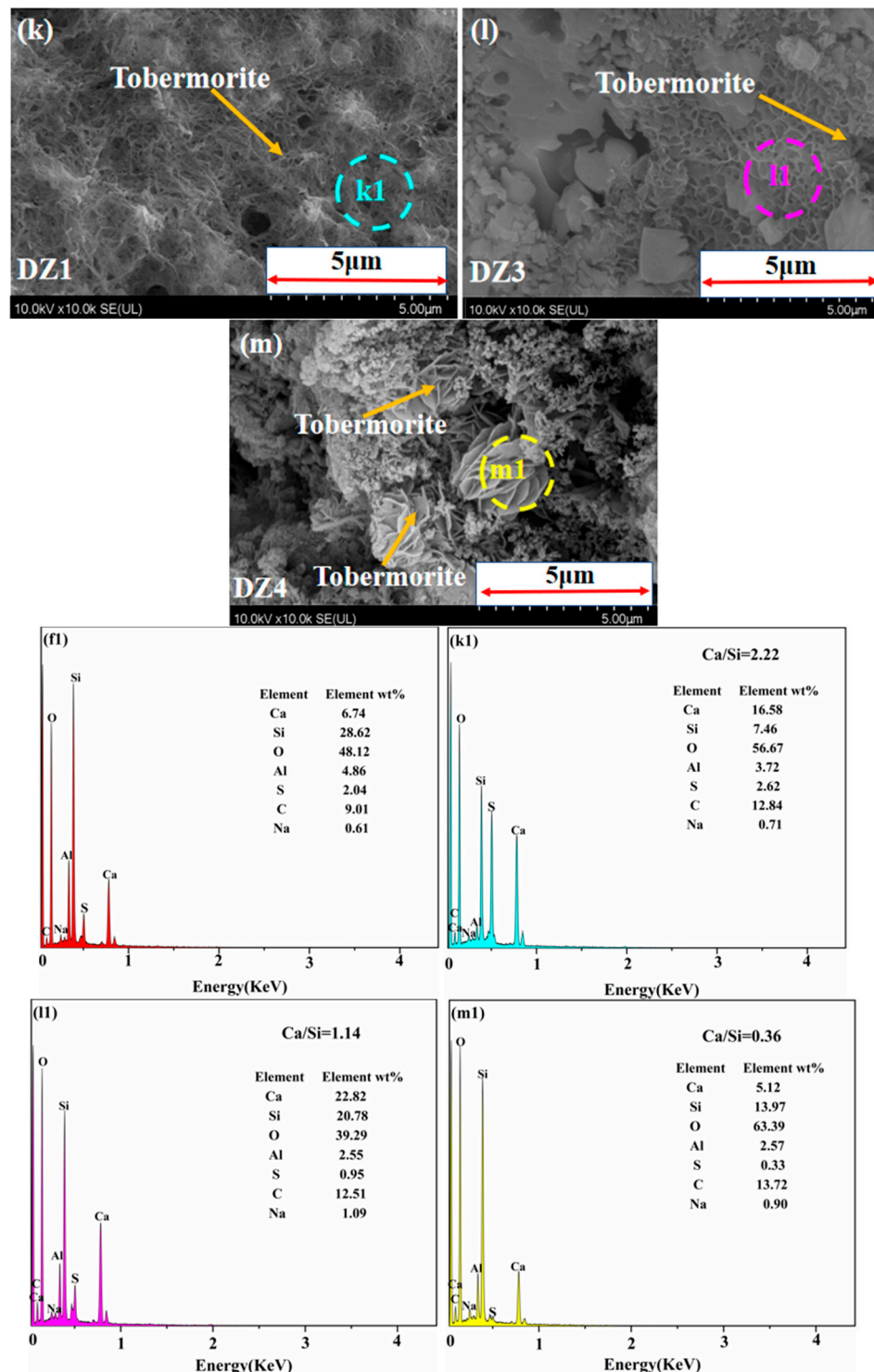


Figure 10. SEM micrographs and EDXS analyses; (a–h): before autoclaving; (i–m): after autoclaving; (f1): the drawn spot in Figure (f); (k1): the drawn spot in Figure (k); (l1): the drawn spot in Figure (l); (m1): the drawn spot in Figure (m).

The images of the AAC after autoclaving are shown in Figure 10i–m. Figure 10i shows the apparent morphology of DZ1. The sample without disused ZSM-5 retained its compact structure after autoclaving, while the surface was covered with flaky anhydrite, which explains why DZ1 has the highest compressive strength. Figure 10j exhibits the appearance of DZ4. The AAC with disused ZSM-5 shows many clear pores, which confirms that the addition of disused ZSM-5 improves the foaming effect of the final products, adjusts

the PG-based AAC from the B07 to B05 level, and increases the application possibilities of the product. The presence of anhydrite and tobermorite ensures the strength of DZ4. The partial micrographs of DZ1, DZ3, and DZ4 are shown in Figure 10k,l,m, respectively, and all samples are covered with a large amount of tobermorite. Notably, the morphologies of the three types of tobermorite are not identical; the tobermorite in DZ1 shows semicrystalline characteristics, while the tobermorite phases in DZ3 and DZ4 are grass-like and ribbon-like, respectively. The calcium-to-silica ratio (Ca/Si) directly influences the morphology of tobermorite. The EDXS results (k1, m1, and l1) show that the Ca/Si ratio decreased, the peak of Si slightly increased, and DZ1 had the highest Ca/Si ratio. Some researchers [11,48,49] observed a similar phenomenon; in general, semicrystalline tobermorite has a high Ca/Si ratio, and grass- and ribbon-like tobermorite has a relatively lower Ca/Si ratio than semicrystalline tobermorite. As the content of disused ZSM-5 increased in the samples, the siliceous materials in the AAC increased, and more siliceous materials were involved in the formation of tobermorite, leading to a decrease in the Ca/Si ratio of the final AAC products, which changed the morphology of tobermorite.

4. Conclusions

This study designed an AAC product by using waste PG and disused ZSM-5, and the effects of disused ZSM-5 on the performance of the PG-based AAC were investigated. The following conclusions could be drawn:

- (1) PG-based AAC has a high bulk density, and the addition of disused ZSM-5 causes a decrease in the bulk density. The compressive strength and bulk density of the DZ4 sample (37.5% disused ZSM-5 and 25% waste PG) were 2.6 MPa and 520 kg/m³, respectively.
- (2) As the disused ZSM-5 content gradually increased, the pore distribution of the samples significantly changed. To be specific, the number of large-diameter pores increased, especially pores larger than 52 µm. These large-diameter pores decrease the strength of the sample while decreasing the bulk density of the AAC, which is the primary reason for adjusting the AAC from the B07 to B05 level.
- (3) As the content of disused ZSM-5 increases in the samples, the siliceous materials in the AAC increase, and more siliceous materials are involved in the formation of tobermorite, leading to a decrease in the Ca/Si of the final AAC products, which changes the morphology of tobermorite.
- (4) The addition of waste PG increases the residual gypsum content in the cement hydration process, which promotes the formation of ettringite.

Author Contributions: H.Z. (Hao Zhou): writing—original draft. J.W.: formal analysis. Y.J.: formal analysis. R.L.: formal analysis. B.M.: methodology. B.Q.: conceptualization. Y.H.: conceptualization, data curation. H.Z. (Houhu Zhang): resources. All authors have read and agreed to the published version of the manuscript.

Funding: The authors thank the special fund project for the development of strategic emerging industries in Jiangsu Province ([20176]1594-41), the National Natural Science Foundation of China (52300175) and the Natural Science Foundation of Jiangsu Province of China (BK20220701), the Special Fund of Chinese Central Government for Basic Scientific Research Operations in commonweal Research Institute (GYZX220301) and Special Fund of Carbon Peak and Carbon Neutrality Research Institute supported by Nanjing Institute of Environmental Sciences, Ministry of Ecology and Environment (ZX2023SZY060).

Data Availability Statement: Data and materials supporting the research are found within the manuscript. Raw data files will be provided by the corresponding author upon request.

Conflicts of Interest: Author Yang Jiang was employed by the company Advanced Green-Materials Institute of China Energy Engineering Corporation. The remaining authors declare that the research was conducted in the absence of any commercial or financial relationships that could be construed as a potential conflict of interest.

References

1. Agwa, I.S.; Zeyad, A.M.; Tayeh, B.A.; Adesina, A.; de Azevedo, A.R.G.; Amin, M.; Hadzima-Nyarko, M. A comprehensive review on the use of sugarcane bagasse ash as a supplementary cementitious material to produce eco-friendly concretes. *Mater. Today Proc.* **2022**, *65*, 688–696. [[CrossRef](#)]
2. Qu, X.; Zhao, X. Previous and present investigations on the components, microstructure and main properties of autoclaved aerated concrete—A review. *Constr. Build. Mater.* **2017**, *135*, 505–516. [[CrossRef](#)]
3. Weiksnar, K.D.; Clavier, K.A.; Laux, S.J.; Townsend, T.G. Influence of Trace Chemical Constituents in Phosphogypsum for Road Base Applications: A Review. *Res. Conserv. Recycl.* **2023**, *199*, 107237. [[CrossRef](#)]
4. Peng, Y.; Liu, Y.; Zhan, B.; Xu, G. Preparation of autoclaved aerated concrete by using graphite tailings as an alternative silica source. *Constr. Build. Mater.* **2021**, *267*, 121792. [[CrossRef](#)]
5. Wongkeo, W.; Thongsanitgarn, P.; Pimraksa, K. Chaipanich Compressive strength, flexural strength and thermal conductivity of autoclaved concrete block made using bottom ash as cement replacement materials. *Mater. Des.* **2021**, *35*, 434–439. [[CrossRef](#)]
6. Kunchariyakun, K.; Asavapisit, S.; Sinyoung, S. Influence of partial sand replacement by black rice husk ash and bagasse ash on properties of autoclaved aerated concrete under different temperatures and times. *Constr. Build. Mater.* **2018**, *173*, 220–227. [[CrossRef](#)]
7. Xia, J.; Chen, Y.; Chen, J.; Li, A.; Chen, T. Preparation of autoclaved aerated concrete from construction waste. *IOP Conf. Ser. Earth Environ. Sci.* **2021**, *687*, 012067. [[CrossRef](#)]
8. Schreiner, J.; Jansen, D.; Ectors, D.; Goetz-Neunhoeffler, F.; Neubauer, J.; Volkmann, S. New analytical possibilities for monitoring the phase development during the production of autoclaved aerated concrete. *Cem. Concr. Res.* **2018**, *107*, 247–252. [[CrossRef](#)]
9. Shams, T.; Schober, G.; Heinz, D.; Seifert, S. Production of autoclaved aerated concrete with silica raw materials of a higher solubility than quartz Part II: Influence of autoclaving temperature. *Constr. Build. Mater.* **2021**, *287*, 123072. [[CrossRef](#)]
10. Yazal, A.; Kavas, T.; Soyal, A.D. Effects of different autoclaving pressure on mechanical properties of AAC. *Ce/Papers* **2018**, *2*, 591–594. [[CrossRef](#)]
11. Jiang, J.; Ma, B.; Cai, Q.; Shao, Z.; Hu, Y.; Qian, B.; Wang, J.; Ma, F.; Wang, L. Utilization of ZSM-5 waste for the preparation of autoclaved aerated concrete (AAC): Mechanical properties and reaction products. *Constr. Build. Mater.* **2021**, *297*, 123821. [[CrossRef](#)]
12. Cai, L.; Ma, B.; Li, X.; Lv, Y.; Liu, Z.; Jian, S. Mechanical and hydration characteristics of autoclaved aerated concrete (AAC) containing iron-tailings: Effect of content and fineness. *Constr. Build. Mater.* **2016**, *128*, 361–372. [[CrossRef](#)]
13. Huang, X.Y.; Ni, W.; Cui, W.H.; Wang, Z.J.; Zhu, L.P. Preparation of autoclaved aerated concrete using copper tailings and blast furnace slag. *Constr. Build. Mater.* **2012**, *27*, 1–5. [[CrossRef](#)]
14. Chen, Y.-L.; Chang, J.-E.; Lai, Y.-C.; Ko, M.-S.; Chen, Y.-H. Recycling of steel slag fines for the production of autoclaved aerated concrete (AAC). *Ce/Papers* **2018**, *2*, 445–449. [[CrossRef](#)]
15. Kamal, M.A. Analysis of autoclaved aerated concrete (AAC) blocks with reference to its potential and sustainability. *J. Build. Mater. Struct.* **2020**, *7*, 76–86. [[CrossRef](#)]
16. Cao, S.; Zheng, D.; Yilmaz, E.; Yin, Z.Y.; Xue, G.L.; Yang, F.D. Strength development and microstructure characteristics of artificial concrete pillar considering fiber type and content effects. *Constr. Build. Mater.* **2020**, *256*, 119408. [[CrossRef](#)]
17. Cao, S.; Xue, G.; Yilmaz, E.; Yin, Z.; Yang, F. Utilizing concrete pillars as an environmental mining practice in underground mines. *J. Clean. Prod.* **2021**, *278*, 123433. [[CrossRef](#)]
18. Ren, K.; Cui, N.; Zhao, S.; Zheng, K.; Ji, X.; Feng, L.; Cheng, X.; Xie, N. Low-carbon sustainable composites from waste phosphogypsum and their environmental impacts. *Crystals* **2021**, *11*, 719. [[CrossRef](#)]
19. Chernysh, Y.; Yakhnenko, O.; Chubur, V.; Roubík, H. Phosphogypsum recycling: A review of environmental issues, current trends, and prospects. *Appl. Sci.* **2021**, *11*, 1575. [[CrossRef](#)]
20. Cuadri, A.A.; Pérez-Moreno, S.; Altamar, C.L.; Navarro, F.J.; Bolívar, J.P. Phosphogypsum as additive for foamed bitumen manufacturing used in asphalt paving. *J. Clean. Prod.* **2021**, *283*, 124661. [[CrossRef](#)]
21. Shen, W.; Zhou, M.; Ma, W.; Hu, J.; Cai, Z. Investigation on the application of steel slag-fly ash-phosphogypsum solidified material as road base material. *J. Hazard. Mater.* **2009**, *164*, 99–104. [[CrossRef](#)] [[PubMed](#)]
22. Yang, J.; Liu, W.; Zhang, L.; Xiao, B. Preparation of load-bearing building materials from autoclaved phosphogypsum. *Constr. Build. Mater.* **2009**, *23*, 687–693. [[CrossRef](#)]
23. Mostafa, N.Y.; Shaltout, A.A.; Omar, H.; Abo-El-Enein, S.A. Hydrothermal synthesis and characterization of aluminium and sulfate substituted 1.1 nm tobermorites. *J. Alloys Compd.* **2009**, *467*, 332–337. [[CrossRef](#)]
24. Rashad, A.M. Potential use of phosphogypsum in alkali-activated fly ash under the effects of elevated temperatures and thermal shock cycles. *J. Clean. Prod.* **2014**, *87*, 717–725. [[CrossRef](#)]
25. Kalpana, M.; Mohith, S. Study on autoclaved aerated concrete: Review. *Mater. Today Proc.* **2019**, *22*, 894–896. [[CrossRef](#)]
26. Xue, W.; Jing, W.; Wang, Z.; Zhang, H.; Lin, J. Mechanical behavior and constitutive model of lining concrete in triaxial compression infiltration process under pore water pressure. *Arch. Civ. Mech. Eng.* **2023**, *23*, 20. [[CrossRef](#)]
27. Groen, J.C.; Zhu, W.; Brouwer, S.; Huynink, S.J.; Kapteijn, F.; Moulijn, J.A.; Pérez-Ramírez, J. Direct demonstration of enhanced diffusion in mesoporous ZSM-5 zeolite obtained via controlled desilication. *J. Am. Chem. Soc.* **2007**, *129*, 355–360. [[CrossRef](#)]
28. Zhang, G.; He, J.; Gambrell, R.P. Synthesis, characterization, and mechanical properties of red mud-based geopolymers. *Transp. Res. Rec.* **2010**, *1*, 1–9. [[CrossRef](#)]

29. Calleja, G.; Pau, J.; Calles, J.A. Pure and multicomponent adsorption equilibrium of carbon dioxide, ethylene, and propane on ZSM-5 zeolites with different Si/Al ratios. *J. Chem. Eng. Data* **1998**, *43*, 994–1003. [[CrossRef](#)]
30. Khunt, Y.; Khamar, N.; Nathwani, V.; Joshi, T.; Dave, U. Investigation on mechanical parameters of concrete having sustainable materials. *Mater. Today. Proc.* **2022**, *66*, 2292–2297. [[CrossRef](#)]
31. Shao, Z.; Ma, B.; Wang, J.; Cai, Q.; Jiang, J.; Qian, B.; Cheng, G.P.; Hu, Y.; Ma, F.; Sun, J.; et al. The influence of ZSM-5 waste on the properties of fly ash-based foamed geopolymer. *J. Clean. Prod.* **2022**, *355*, 131800. [[CrossRef](#)]
32. Peng, P.; Wang, Y.; Zhang, Z.; Qiao, K.; Liu, X.; Yan, Z.; Subhan, F.; Komarneni, S. ZSM-5-based mesostructures by combined alkali dissolution and re-assembly: Process controlling and scale-up. *Chem. Eng. J.* **2016**, *302*, 323–333. [[CrossRef](#)]
33. Zhu, H.; Liang, G.; Zhang, Z.; Wu, Q.; Du, J. Partial replacement of metakaolin with thermally treated rice husk ash in metakaolin-based geopolymer. *Constr. Build. Mater.* **2019**, *221*, 527–538. [[CrossRef](#)]
34. al Bakri Abdullah, M.M.; Hussin, K.; Bnhussain, M.; Ismail, K.N.; Yahya, Z.; Razak, R.A. Fly ash-based geopolymer lightweight concrete using foaming agent. *Int. J. Mol. Sci.* **2012**, *13*, 7186–7198. [[CrossRef](#)] [[PubMed](#)]
35. Wan, D.; Zhang, W.; Tao, Y.; Wan, Z.; Wang, F.; Hu, S.; He, Y. The impact of Fe dosage on the ettringite formation during high ferrite cement hydration. *J. Am. Ceram. Soc.* **2021**, *104*, 3652–3664. [[CrossRef](#)]
36. Chen, J.K.; Jiang, M.Q. Long-term evolution of delayed ettringite and gypsum in Portland cement mortars under sulfate erosion. *Constr. Build. Mater.* **2009**, *23*, 812–816. [[CrossRef](#)]
37. Gil, B.; Mokrzycki, L.; Sulikowski, B.; Olejniczak, Z.; Walas, S. Desilication of ZSM-5 and ZSM-12 zeolites: Impact on textural, acidic and catalytic properties. *Catal. Today* **2010**, *152*, 24–32. [[CrossRef](#)]
38. Khatib, J.M.; Mangat, P.S.; Wright, L. Pore size distribution of cement pastes containing fly ash-gypsum blends cured for 7 days. *KSCE J. Civ. Eng.* **2014**, *18*, 1091–1096. [[CrossRef](#)]
39. Reddy, B.V.V.; Gourav, K. Strength of lime-fly ash compacts using different curing techniques and gypsum additive. *Mater. Struct.* **2011**, *44*, 1793–1808. [[CrossRef](#)]
40. Mingliang, Q.; Shuaiqi, T.; Liwu, F.; Zitao, Y.; Jian, G. Thermal Conductivity of Silica-aerogel (SA) and Autoclave Aerated Concrete (AAC) Composites. *E3S Web Conf.* **2022**, *172*, 21007. [[CrossRef](#)]
41. Chen, Y.L.; Chang, J.E.; Lai, Y.C.; Chou, M.I.M. A comprehensive study on the production of autoclaved aerated concrete: Effects of silica-lime-cement composition and autoclaving conditions. *Constr. Build. Mater.* **2017**, *153*, 622–629. [[CrossRef](#)]
42. di Wu, R.; Dai, S.B.; Jian, S.W.; Huang, J.; Lv, Y.; Li, B.D.; Azizbek, N. Utilization of the circulating fluidized bed combustion ash in autoclaved aerated concrete: Effect of superplasticizer. *Constr. Build. Mater.* **2020**, *237*, 117644.
43. Xue, W.; Twenda, C.; Alam, M.S.; Xu, L.; Wang, Z. Experimental study on seepage characteristics and stress sensitivity of desulfurization gypsum based concrete under triaxial stress. *J. Mater. Res. Technol.* **2023**, *24*, 6425–6437. [[CrossRef](#)]
44. Sun, D.; Yin, F.; Deng, Y.; Liu, K.; Tang, J.; Shen, C.; Sun, Y.; Wang, A.; Huang, N.; Hu, C. Utilization of carbide slag in autoclaved aerated concrete (CS-AAC) and optimization: Foaming, hydration process, and physic-mechanical properties. *Case Stud. Constr. Mater.* **2023**, *19*, e02354. [[CrossRef](#)]
45. Gao, K.; Lin, K.L.; Wang, D.; Hwang, C.L.; Shiu, H.S.; Chang, Y.M.; Cheng, T.W. Effects SiO₂/Na₂O molar ratio on mechanical properties and the microstructure of nano-SiO₂ metakaolin-based geopolymers. *Constr. Build. Mater.* **2014**, *53*, 503–510. [[CrossRef](#)]
46. Heah, C.Y.; Kamarudin, H.; Al Bakri, A.M.M.; Bnhussain, M.; Luqman, M.; Nizar, I.K.; Ruzaidi, C.M.; Liew, Y.M. Study on solids-to-liquid and alkaline activator ratios on kaolin-based geopolymers. *Constr. Build. Mater.* **2012**, *35*, 912–922. [[CrossRef](#)]
47. Zhao, W.; Yang, H.; Huo, C. Surface nanocrystallization modification of anhydrite. *Colloids Surf. A Physicochem. Eng. Asp.* **2012**, *393*, 128–132. [[CrossRef](#)]
48. Ayeni, O.; Onwualu, A.P.; Boakye, E. Characterization and mechanical performance of metakaolin-based geopolymer for sustainable building applications. *Constr. Build. Mater.* **2021**, *272*, 121938. [[CrossRef](#)]
49. Kunchariyakun, K.; Asavapisit, S.; Sombatsompop, K. Properties of autoclaved aerated concrete incorporating rice husk ash as partial replacement for fine aggregate. *Cem. Concr. Compos.* **2015**, *55*, 11–16. [[CrossRef](#)]

Disclaimer/Publisher’s Note: The statements, opinions and data contained in all publications are solely those of the individual author(s) and contributor(s) and not of MDPI and/or the editor(s). MDPI and/or the editor(s) disclaim responsibility for any injury to people or property resulting from any ideas, methods, instructions or products referred to in the content.